

RESEARCH ARTICLE

# Analysis and numerical simulation of a supercell tornado at the Hong Kong adjacent waters

P. W. Chan<sup>1</sup>  | K. K. Hon<sup>1</sup>  | P. Robinson<sup>2</sup> | K. Kosiba<sup>2</sup> | J. Wurman<sup>3</sup> | Q. S. Li<sup>4</sup>

<sup>1</sup>Hong Kong Observatory, Kowloon, Hong Kong, China

<sup>2</sup>Targeted Meteorological Systems, Boulder, Colorado, USA

<sup>3</sup>Center for Severe Weather Research, Boulder, Colorado, USA

<sup>4</sup>Department of Architecture and Civil Engineering, City University of Hong Kong, Kowloon, Hong Kong, China

## Correspondence

P. W. Chan, Hong Kong Observatory, 134A Nathan Road, Kowloon, Hong Kong, China.  
Email: pwchan@hko.gov.hk

## Abstract

A tornado/waterspout associated with a supercell thunderstorm was observed in the adjacent waters of southern China on the evening of 18 April 2019. The case was documented using surface weather observations and Doppler radar data. A weather station near the tornado/waterspout, recorded wind gusts corresponding to hurricane intensity for a few seconds, never observed before in the region. The Doppler velocity associated with the tornado/waterspout was analysed and the vertical profile of the velocity could be very useful for wind engineering applications in the region. Dual-polarization observations also were analysed and exhibited some similar signatures documented in supercell tornadoes in other parts of the world. Predictability of the tornado/waterspout was studied using a numerical weather prediction model. It showed that the location and timing of the waterspout/tornado could be roughly reproduced, and the model might be used to give earlier alerting to the vessels operating in the south China coastal waters.

## KEYWORDS

forecasting, modelling, remote sensing

## 1 | INTRODUCTION

Tornadoes are not commonly observed in southern China. In Hong Kong, since 1982, there have been only 10 visual reports of tornadoes based on records from the Hong Kong Observatory (HKO). The last such report was in 2005. According to Chen et al. (2017), there are about 20–30 tornadoes over southern China in a study period of 64 years (1948–2012), indicating that waterspouts/tornadoes are not very common in south China coastal areas. Many of the tornadoes are associated with isolated thunderstorms in rainy weather (e.g. active southwest monsoon) and the outer rain-bands associated with tropical cyclones.

On 18 April 2019, a tornado occurred to the southwest of Hong Kong and moved toward the eastsoutheast. According to the wind record of an island weather station impacted by the tornado, a wind gust of 44.2 m/s was recorded, the winds briefly reaching hurricane intensity. Weather radar indicated that this storm had a hook-shaped echo and it is surmised that this tornado was associated with a supercell. To the best of the authors' knowledge, this is the first supercell-associated tornado reported in the region. The event is exceptionally rare and deserves proper documentation for reference by the weather forecasters of southern China and by researchers of tornadoes.

This is an open access article under the terms of the Creative Commons Attribution License, which permits use, distribution and reproduction in any medium, provided the original work is properly cited.

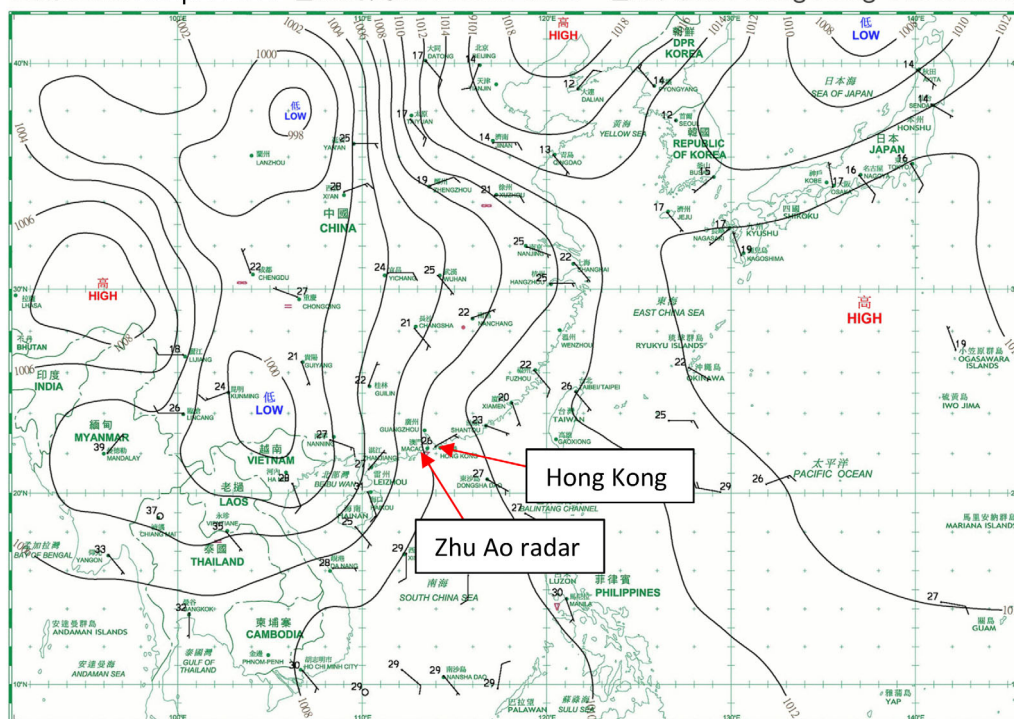
© 2022 The Authors. *Meteorological Applications* published by John Wiley & Sons Ltd on behalf of Royal Meteorological Society.

According to news reports, the supercell might have contributed to the sinking of a vessel over south China coastal waters. The report by the Marine Department of the Hong Kong Government is available at [https://www.mardep.gov.hk/en/publication/publications/reports/mai\\_](https://www.mardep.gov.hk/en/publication/publications/reports/mai_)

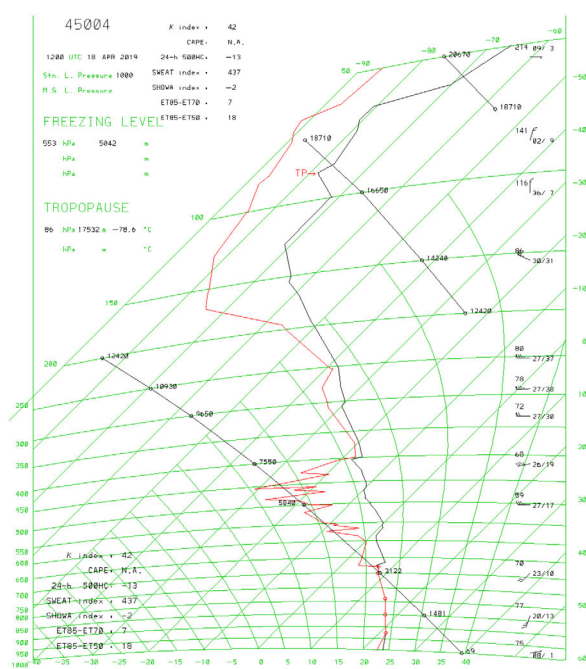
report2019.html, with a summary in English and a full report in Chinese only.

This paper has the following structure. The synoptic setup and atmospheric environment are described in Section 2. The preliminary analysis of the surface, radar

日期/Date: 18 April 2019 香港時間/HK Time: 20:00 香港天文台 Hong Kong Observatory



(a)



(b)

FIGURE 1 (a) The surface isobaric chart at 12 UTC, 18 April 2018. (b) The sounding at 12 UTC

and lightning observations is given in Section 3. The radar data are then analysed in more detail, including a Ground-Based Velocity Track Display (GBVTD) analysis in Section 4 and the storm characteristics from dual-

polarization radar observation are given in Section 5. The results of the numerical weather prediction model are discussed in Section 6 and the conclusions are drawn in Section 7.

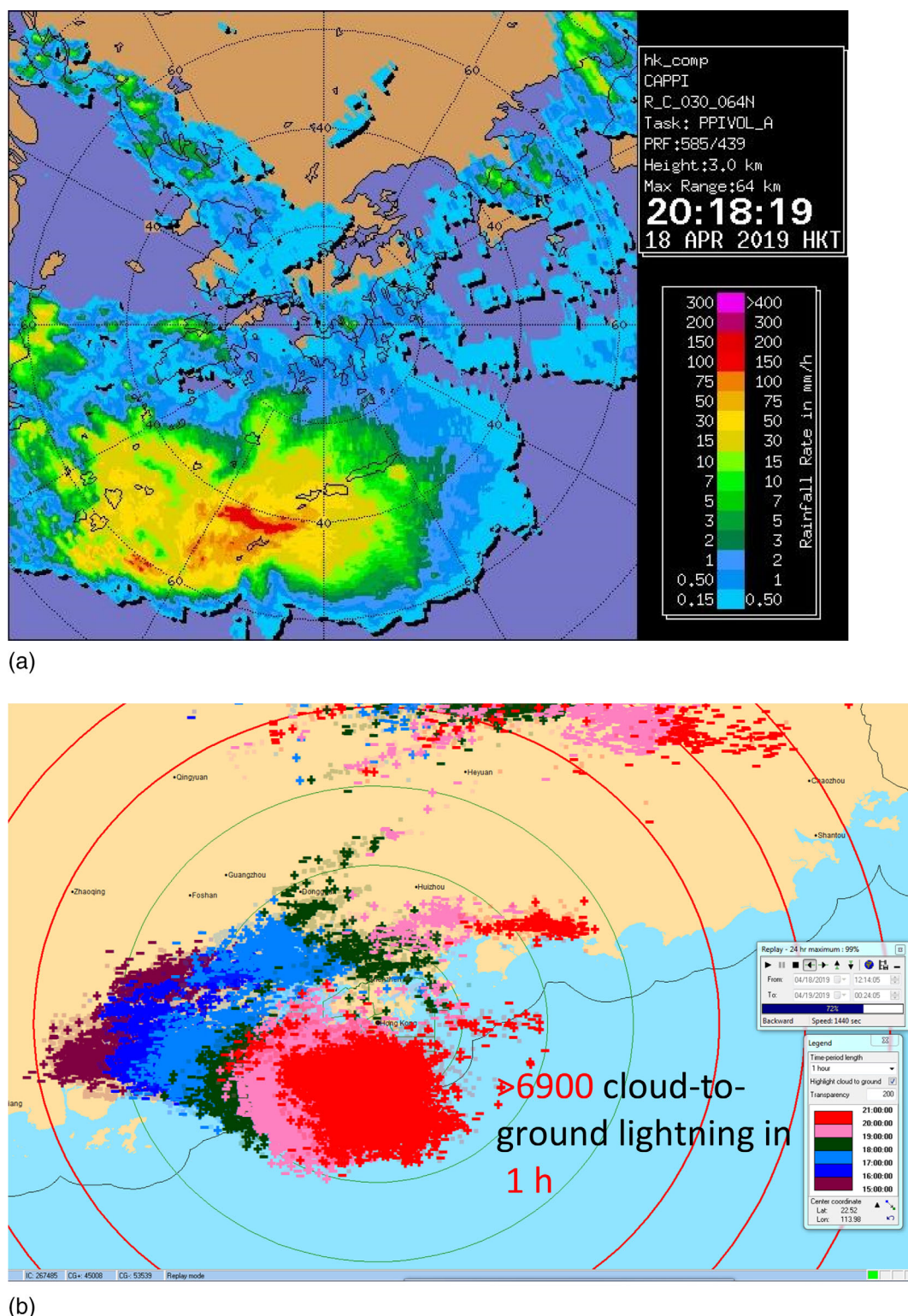


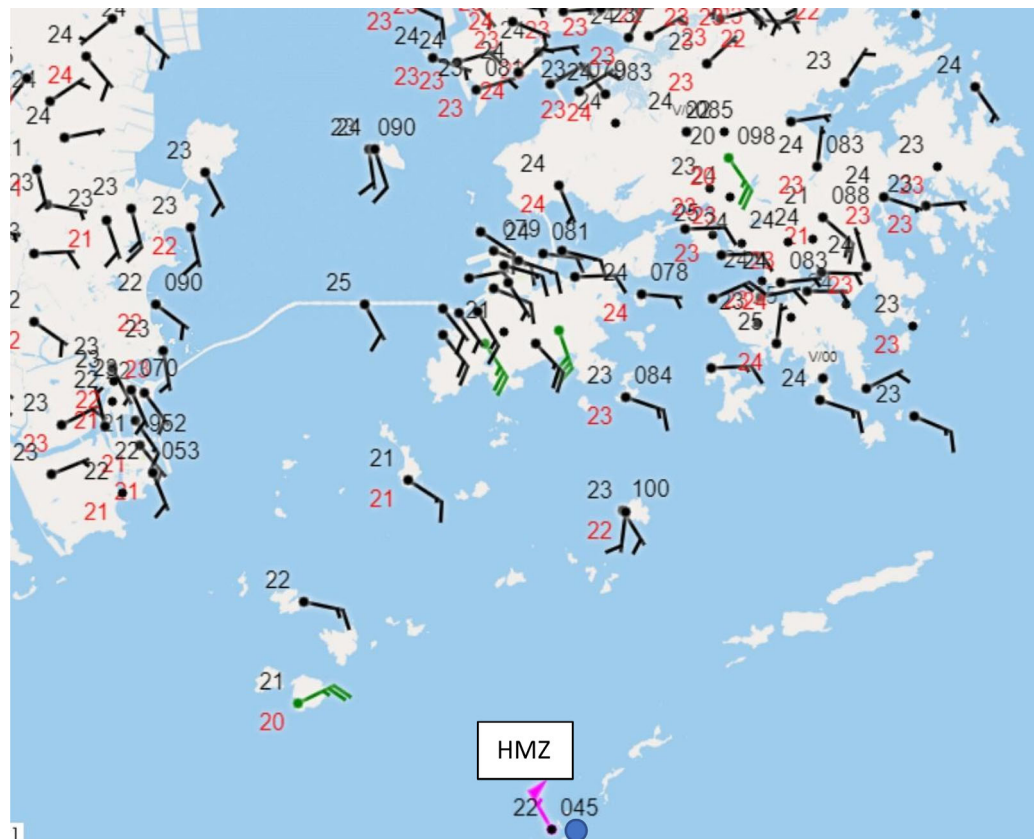
**FIGURE 2** (a) The 3-km reflectivity from Zhu Ao radar at 12:18 UTC. The hourly cloud-to-ground lightning strikes between 07 UTC (15 H) and 13 UTC (21 H) are shown in (b) and total over 6900 counts in 1 h



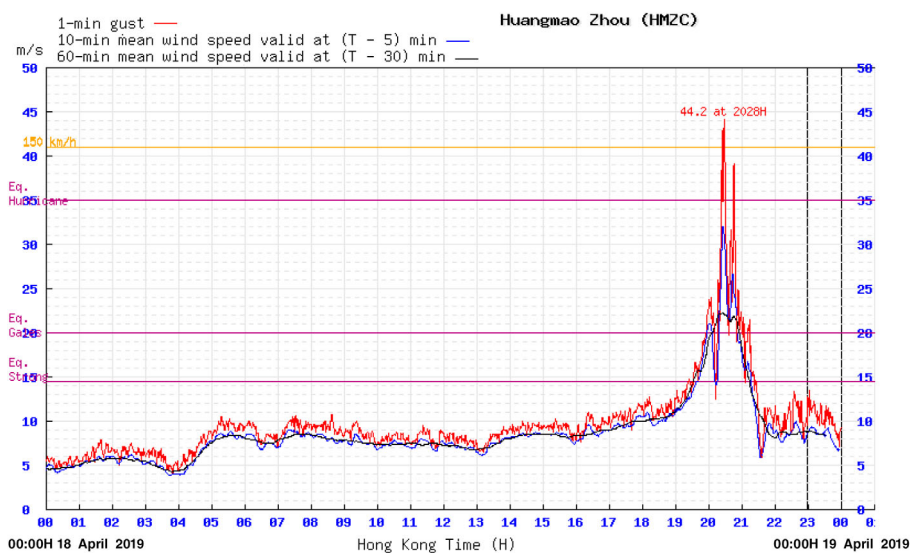
## 2 | SYNOPTIC BACKGROUND

An active southwest monsoon brought unsettled weather to the region. From the surface synoptic chart at 12 UTC

(8 PM local time, with Hong Kong time = UTC + 8 h), 18 April 2019, a south to south-easterly flow prevailed over the southern China (Figure 1a), and a strong pressure gradient existed at the surface.



(a)



(b)

**FIGURE 3** (a) The 10-min mean winds near the supercell (blue dot) at 12:35 UTC. The times series of the wind at Huang Mao Zhou is shown in (b)



**FIGURE 4** The reflectivity (upper) and Doppler velocity (lower) images at 11:08 UTC. The lower panel shows the waterspout/tornado embedded in the larger supercell (in lower left quadrant of image). The upper panel shows the associated reflectivity ring

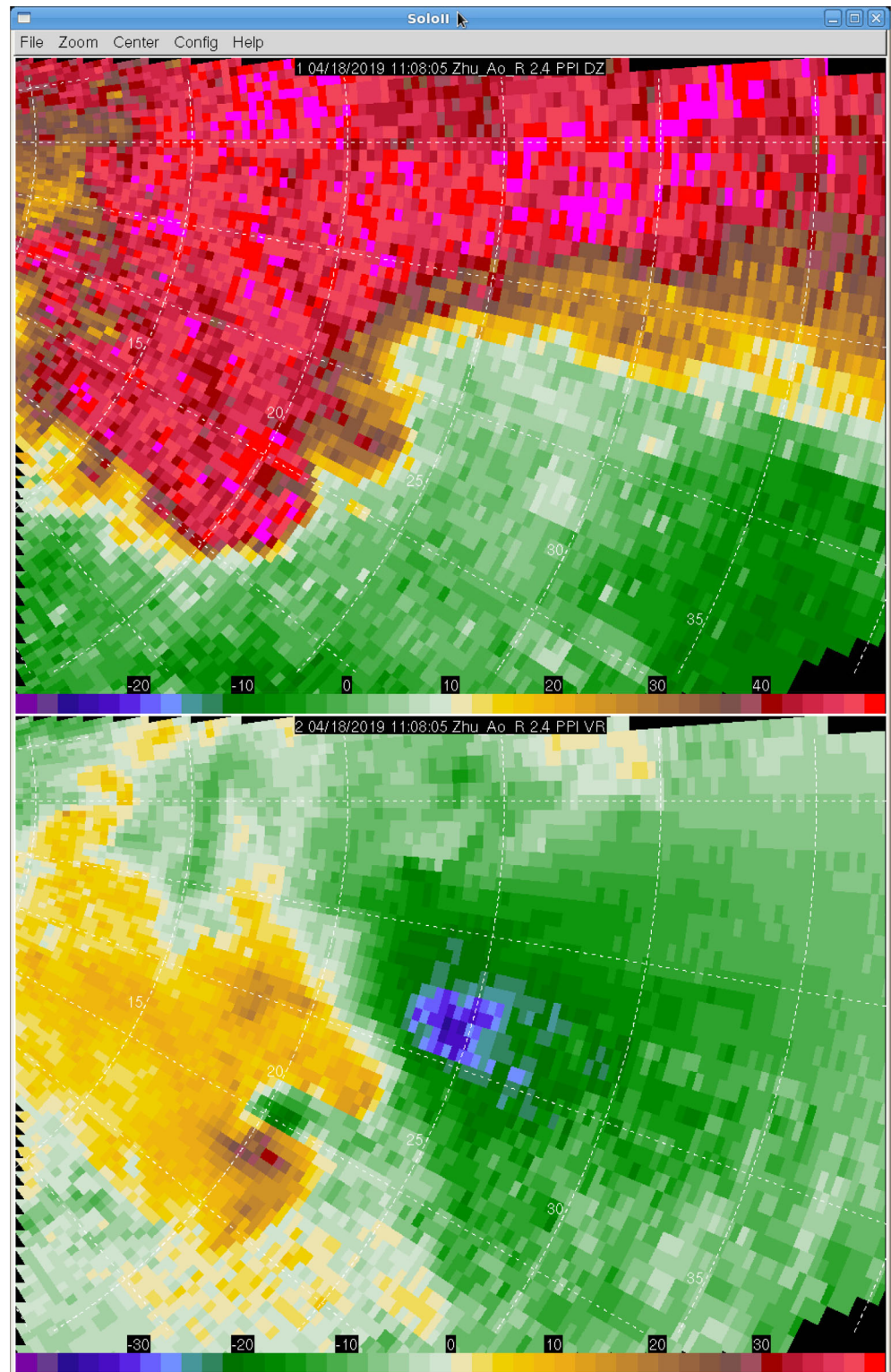


**TABLE 1** Properties of the small vortex

Time	Range (km)	Doppler velocity (m/s)	Diameter (m)
11:00	18.8	15.1	1000
11:07	20.3	41.5	1430
11:13	25.25	41.5	880

The 12Z upper-air sounding from Hong Kong is given in Figure 1b in the form of a tephigram. The atmosphere was very humid. The K index was  $42^\circ$ , indicating a very unstable atmosphere. In this instance, the surface-based convective available potential energy could not be calculated possibly due to the stabilizing effect of the cooler atmospheric boundary layer in rain.

### 3 | PRELIMINARY ANALYSIS OF THE SURFACE, RADAR AND LIGHTNING OBSERVATIONS

The HKO and the other meteorological authorities in the region operate a dense network of surface weather stations over the Pearl River Estuary. These automatic weather stations measure surface wind, temperature, dew point and pressure at a frequency of once 1 min/10 min. The present analyses focus on the weather observations from an island station called Huang Mao Zhou (HMZ), which is located about 50 km to the south-southwest of Hong Kong (Figure 3a).

Several Doppler weather radars with dual-polarization capabilities are operated by the meteorological authorities in the region. This paper analyses the data from the radar at Zhu Ao, (location in Figure 1a). The Zhu Ao radar is installed on the top of a small hill near the Jin Wan Airport of Zhuhai. The site ( $22^\circ 1.6'N$ ,  $113^\circ 22.2'E$ ) is about 26 km to the southwest of Macau and has an elevation of about 255 m above sea level. The radar is a dual-polarization S-band radar operating at a wavelength of about 10.3 cm. The maximum unambiguous radial velocity (or Nyquist velocity) is about 51 m/s.

In addition to the Zhu Ao, the meteorological authorities of Guangdong Province, Hong Kong and Macau jointly operate a lightning detection network in the region. The network consists of nine sensor stations spread over Hong Kong (including Chung Hom Kok, Tsim Bei Tsui, Sha Tau Kok and Chek Lap Kok), Guangdong (including Sanshui, Huidong, Yangjiang and Dongao Island, Zhuhai) and Macau (Taipa). More information on the lightning location network can be found in Lam et al. (2018). According to the publicly available information ([https://www.hko.gov.hk/en/wxinfo/llis/gm\\_index.htm](https://www.hko.gov.hk/en/wxinfo/llis/gm_index.htm)), its accuracy in determining the location of cloud-to-ground lightning strokes is about 250 m within the network when all stations are operational, while the lightning detection efficiency is estimated to reach 95% for cloud-to-ground lightning and more than 50% for cloud-to-cloud lightning.

Radar data show that a storm with supercell characteristics moved across the area generally from west to east. The storm was isolated, had a hook-like reflectivity feature (Figure 2a) and a large mesocyclone with at least one smaller vortex apparent in the Doppler velocity (DV) data. Lightning was very frequent in association with this storm. The hourly lightning location data were shown in Figure 2b. There were generally several thousand cloud-to-ground lightning strikes per hour.

The surface observations in association with the storm are shown in Figure 3. Figure 3a shows the surface observations over the Pearl River Estuary at about 12:35 UTC. The 10-min mean winds are shown. The winds near the waterspout/tornado were more than 50 kn as recorded at a station called HMZ. The time series of the winds at HMZ is shown in Figure 3b. The 3-s gust reached 44.2 m/s. Such a gust had never been observed

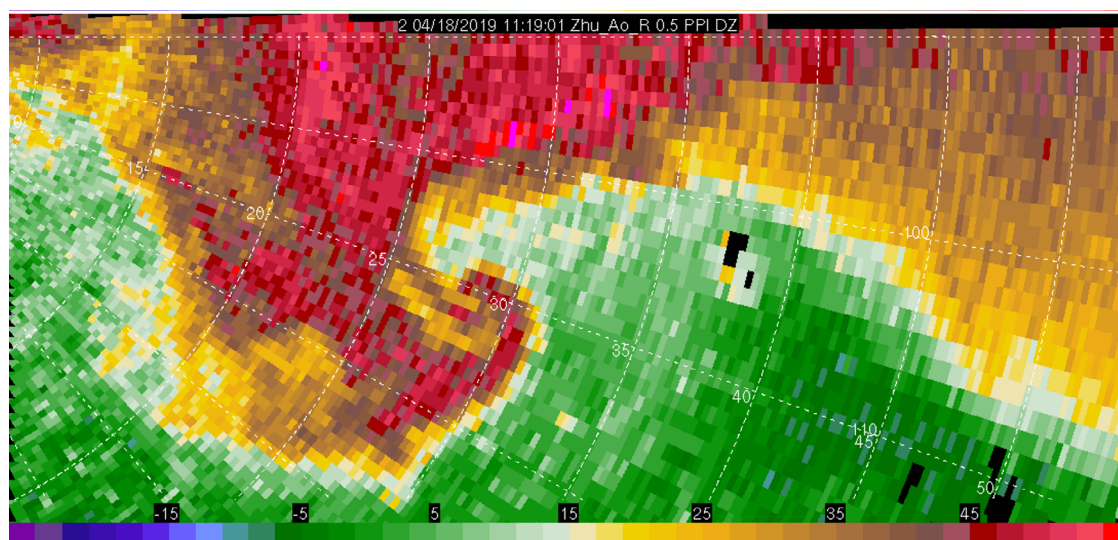
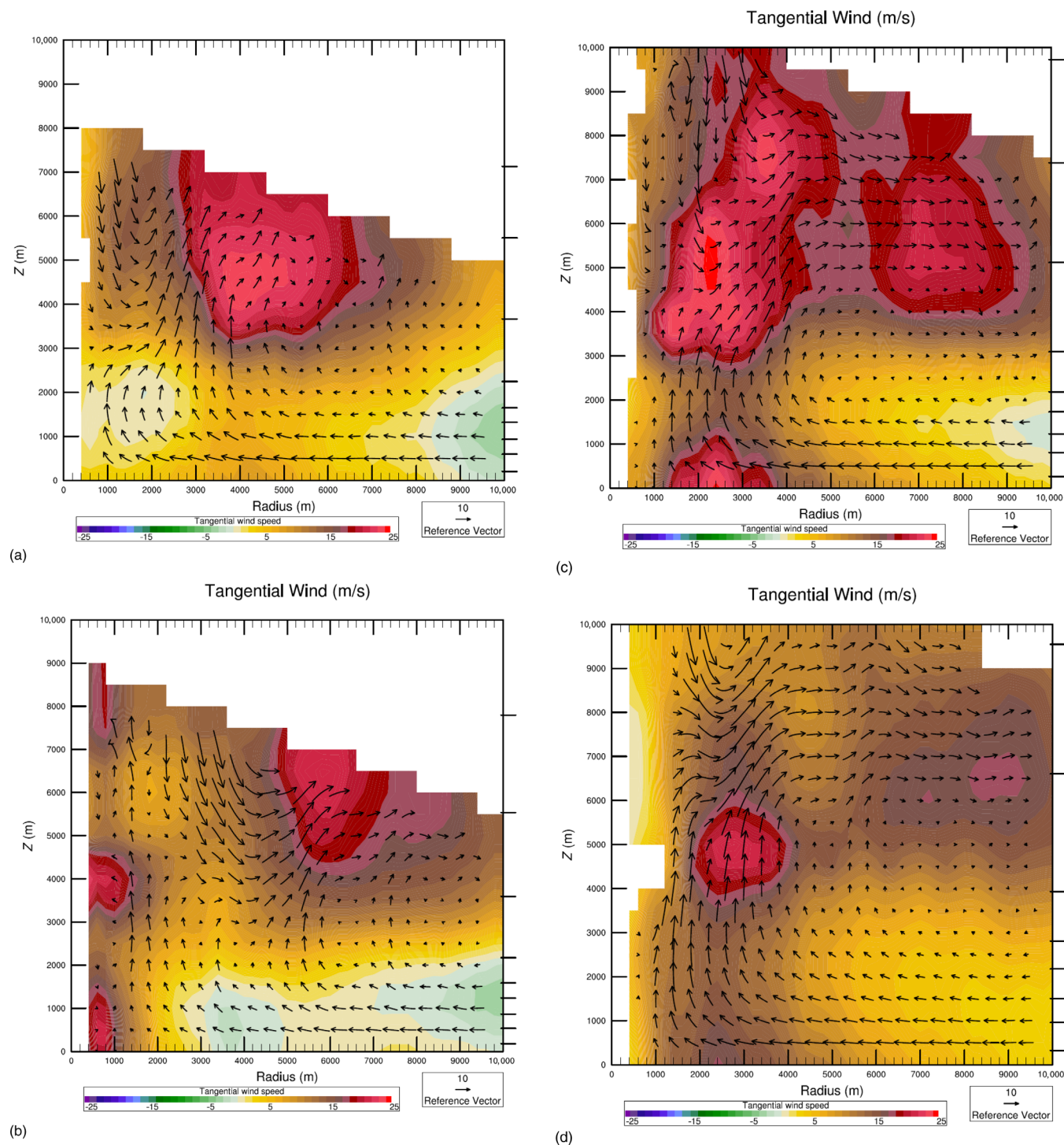


FIGURE 5 Radar reflectivity data showing the storm during its strongest phase at 11:19 UTC





**FIGURE 6** (a) The Ground-Based Velocity Track Display (GBVTD) result for 11:07 UTC centred on the mesocyclone. Tangential speed (colours) and radial/vertical wind (vectors) are shown as a function of distance from vortex centre, and height. Tick marks along the right vertical axis show the height of radar data used to construct GBVTD analysis. (b) As in (a) but centred on the small vortex. (c,d) The mesocyclone at 11:19 UTC and 11:31 UTC, respectively

before in association with a thunderstorm in the region, apart from tropical cyclones.

The Zhu Ao radar observation of reflectivity and DV is shown in Figure 4a,b, respectively. It can be seen that a small vortex was embedded in the mesocyclone.

The diameter of the mesocyclone was about 5 km and had a maximum differential DV of 70 m/s. A smaller vortex, less than 2 km in diameter, had a DV over 41 m/s. A ring-like reflectivity feature was also observed in the region, at about 11:08 UTC. Table 1



gives DV and the diameter of the small vortex from radar data in the lowest sweep. The large range of this feature likely reduced the intensity of the observed DV. The small vortex disappeared from the data after 11:13 UTC. It is possible that this was the waterspout witnessed in the area.

At the peak intensity, at about 11:19 UTC, a well-defined hook-shaped reflectivity core and mesocyclone were observed (Figure 5), indicative of supercell storm morphology. The tornado was believed to be associated with a supercell.

## 4 | GBVTD ANALYSIS

The GBVTD single Doppler analysis technique (Lee et al., 1999) was used to retrieve an axisymmetric profile of the tangential winds, as well as the secondary circulation (radial and vertical winds) as a function of distance from the centre of the vortex and height.

The mesocyclone was strongest around 11:19. Therefore, the volume at the time of peak intensity and the volumes before and after were chosen for analysis. Three volumes of radar data were edited for GBVTD analysis:

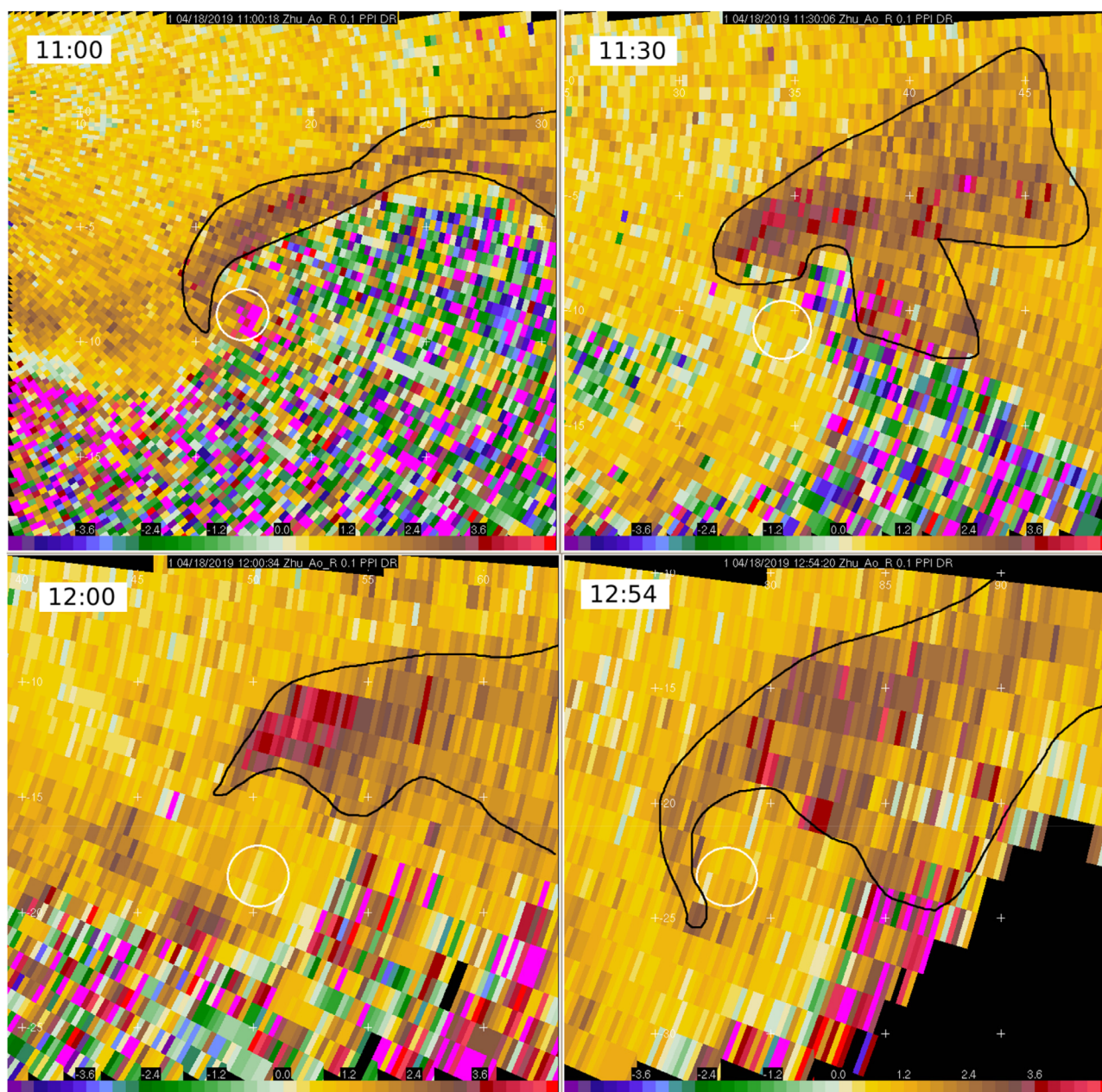


**FIGURE 7** Subjectively determined  $Z_{DR}$  arc (black outline) at various times. There are other areas of enhanced  $Z_{DR}$  values west of the arc, which may also be due to size sorting, but are not contiguous with the arc. The location of the mesocyclone is denoted by the white circle. Tick marks 5 km



11:07, 11:19 and 11:31. The volumes each consisted of 9 sweeps ranging in elevation from  $0.5^\circ$  to  $19.5^\circ$ .

The GBVTD analysis was conducted over a radius of 10 km from the mesocyclone centre and from the small vortex centre to a height of 10 km above ground to show the structure of the mesocyclone and its relation to the smaller vortex. Plots of the results show the vortex-centric average (axisymmetric) tangential (circulation) speed as colours, with the radial and vertical wind shown as vectors. The left vertical axis represents the centre of the vortex.

Results for 11:07 are shown separately for the smaller vortex and for the mesocyclone. Figure 6a shows GBVTD results for the mesocyclone at 11:07. It shows the strongest tangential winds above 4000 m and nearly 25 m/s. The wind field near the ground has a strong radial component toward the centre of the mesocyclone, and then turns upward near centre. The green colours at ranges greater than 8 km indicate that, on average around the mesocyclone, the winds circulate anticyclonically. Within the radius of maximum winds, air descends, but not all the way down to the ground.

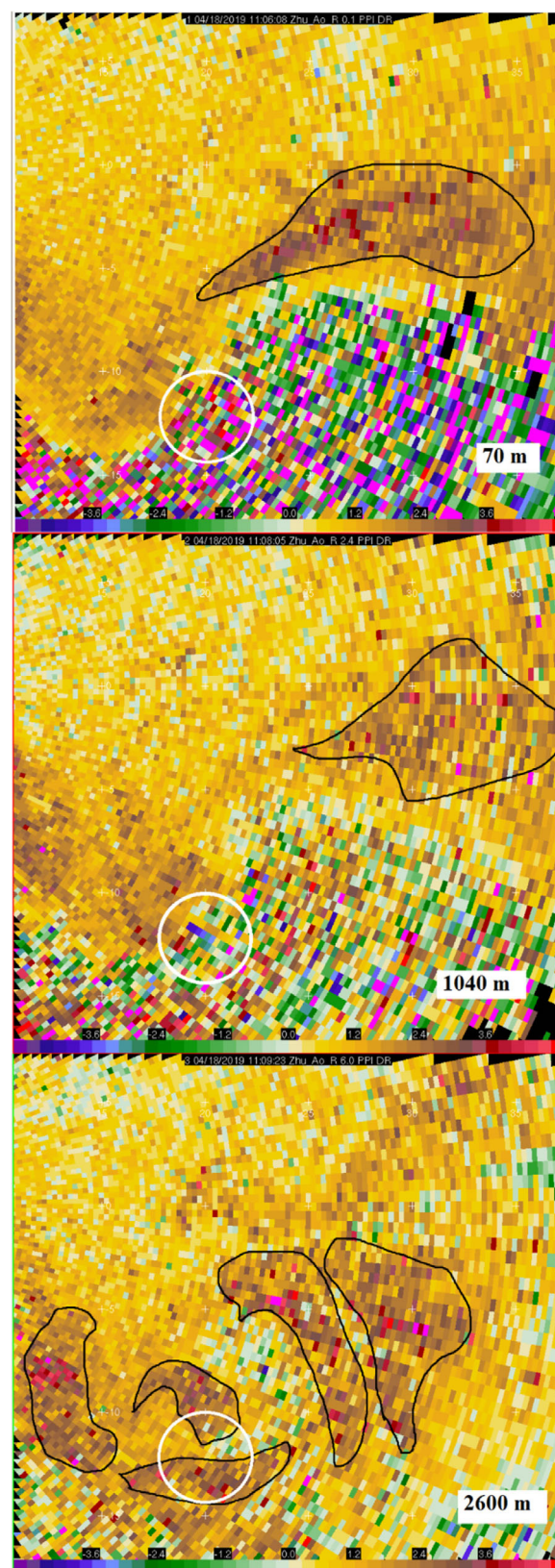
Figure 6b shows GBVTD results for the same volume, but centred on the small vortex. The tornadic circulation is about 700 m in radius and exceeds 20 m/s near ground level, which is consistent with  $DV = 41.5$  m/s at this time in the raw DV data. The low-level radial wind is toward the centre inside the radius of maximum winds. At low-levels, at ranges greater than 3 km from the vortex, the tangential winds are anticyclonic and may have been advected radially inward. This may be the reason this vortex did not last much past 11:13, although there is some evidence that the small vortex may have moved to the centre of the mesocyclone and been ingested by it.

Figure 6c shows GBVTD results for the mesocyclone at 11:19, its most intense phase. Stronger tangential winds are present at ground level with speeds near 25 m/s at a radius of 2400 m. Given the inherent smoothing effect of the GBVTD analysis, the winds shown could be strong enough to cause problems for any boats in that area. The small vortex present earlier may have moved to near the centre of the mesocyclone enhancing its central regions. The upper-level strong circulation region has narrowed too and strengthened to exceed 25 m/s.

Figure 6d shows GBVTD results for the mesocyclone at 11:31. Though the structure is similar to that of 11:19, winds are weaker everywhere.

## 5 | STORM MORPHOLOGY AND DUAL-POLARIZATION SIGNATURES

Analysis of the dual-polarization signatures provides additional insight into internal storm processes. A



**FIGURE 8** Variation of  $Z_{DR}$  in this storm with height. Heights above radar level (ARL) indicated. The subjectively determined  $Z_{DR}$  arc (black outline) is clearly visible at 70 m ARL, near the centre of image, but fades and becomes ring-like with height. The mesocyclone surface location is shown as white circle. Tick marks 5 km



survey of dual-polarization characteristics in supercell storms (Kumjian & Ryzhkov, 2008) identified several common signatures that can be linked to storm processes and/or the near storm environment. While many studies have focused on the identification of these signatures in Great Plains tornadic supercells, recent studies have begun to focus on the relative locations of dual-polarization signatures in non-supercellular tornadic storms (e.g. Loeffler & Kumjian, 2018) and tornadoes produced from tropical cyclones (Crowe et al., 2010; Martinaitis, 2017).

## 5.1 | $Z_{DR}$ arc and $K_{DP}$ foot

The ' $Z_{DR}$  arc' is an arc-shaped area of enhanced differential reflectivity ( $Z_{DR}$ ) along the inflow region of the forward flank. This shallow, low-level feature has been attributed to size sorting of hydrometeors that can be maintained by updrafts and the presence of vertical wind shear (Kumjian & Ryzhkov, 2012) and/or non-zero storm-relative winds in the hydrometeor size sorting layer (Dawson II et al., 2015). In the present case, a  $Z_{DR}$  arc is evident during the entire time span of the available

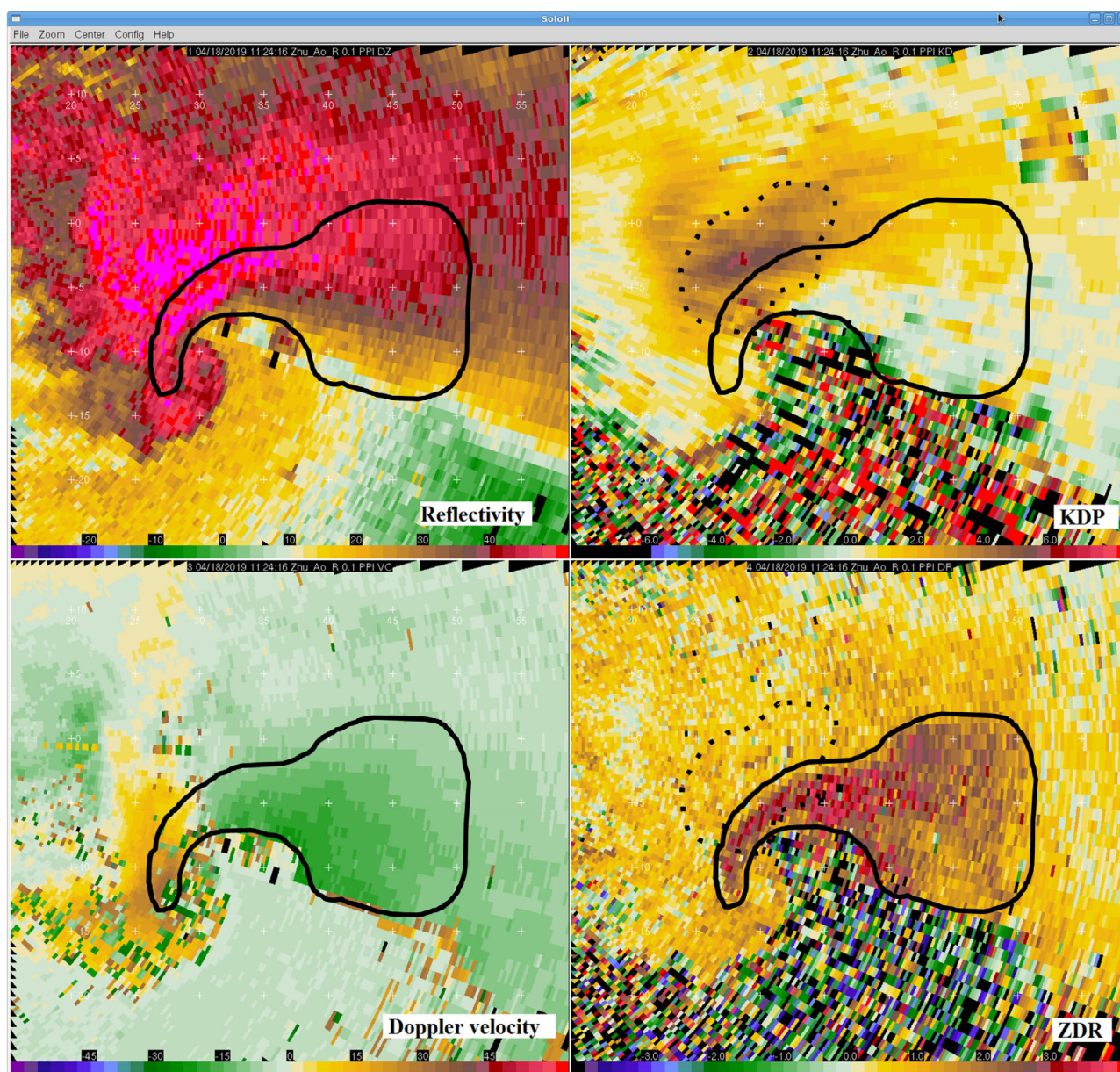


**FIGURE 9** Demonstration of separation of  $K_{DP}$  maximum and  $Z_{DR}$  arc at low-levels (about 60 m above radar level), along with the relationship with other fields at 11:24, when the reflectivity coil was particularly well-formed. The area of enhanced  $K_{DP}$  is about 5 km NW of the  $Z_{DR}$  arc. The  $Z_{DR}$  arc is subjectively outlined in solid black and the maximum in  $K_{DP}$  is denoted by the dotted black boundary



data (11:00–13:00) as an enhancement of  $Z_{DR}$  of up to about 3 dB above the background (Figure 7), but the exact enhancement can vary as a function of radar wavelength and calibration. The  $Z_{DR}$  arc decays slowly with height and becomes ring-like, surrounding the mesocyclone DV couplet above about 3 km above radar level (ARL). Figure 8 shows an example of the variation of the  $Z_{DR}$  arc with height in this storm.

The presence of enhanced  $K_{DP}$  forms in areas of mixed phase precipitation may result from water being shed off of large hail. At low-levels, when analysed in tandem with a  $Z_{DR}$  arc, the offset of a region of enhanced  $K_{DP}$  (a ' $K_{DP}$  foot') from the  $Z_{DR}$  arc can help diagnose low-level storm-relative winds. In the present case, the

$K_{DP}$  maximum is offset about 5 km to the NW of the location of the  $Z_{DR}$  arc as shown in Figure 9, indicating non-zero storm-relative helicity.

## 5.2 | $Z_{DR}$ and $\rho_{HV}$ rings aloft

Ring-like patterns of enhancement in  $Z_{DR}$  and of reduction of correlation coefficient, the correlation between reflectivity factors at horizontal and vertical polarizations ( $\rho_{HV}$ ) aloft indicate an updraft, which, by its warmer temperature, can locally lift the freezing level and lift small debris and hail. Rings may also be enhanced by the cyclonic rotation of the mesocyclone. A  $\rho_{HV}$  depression

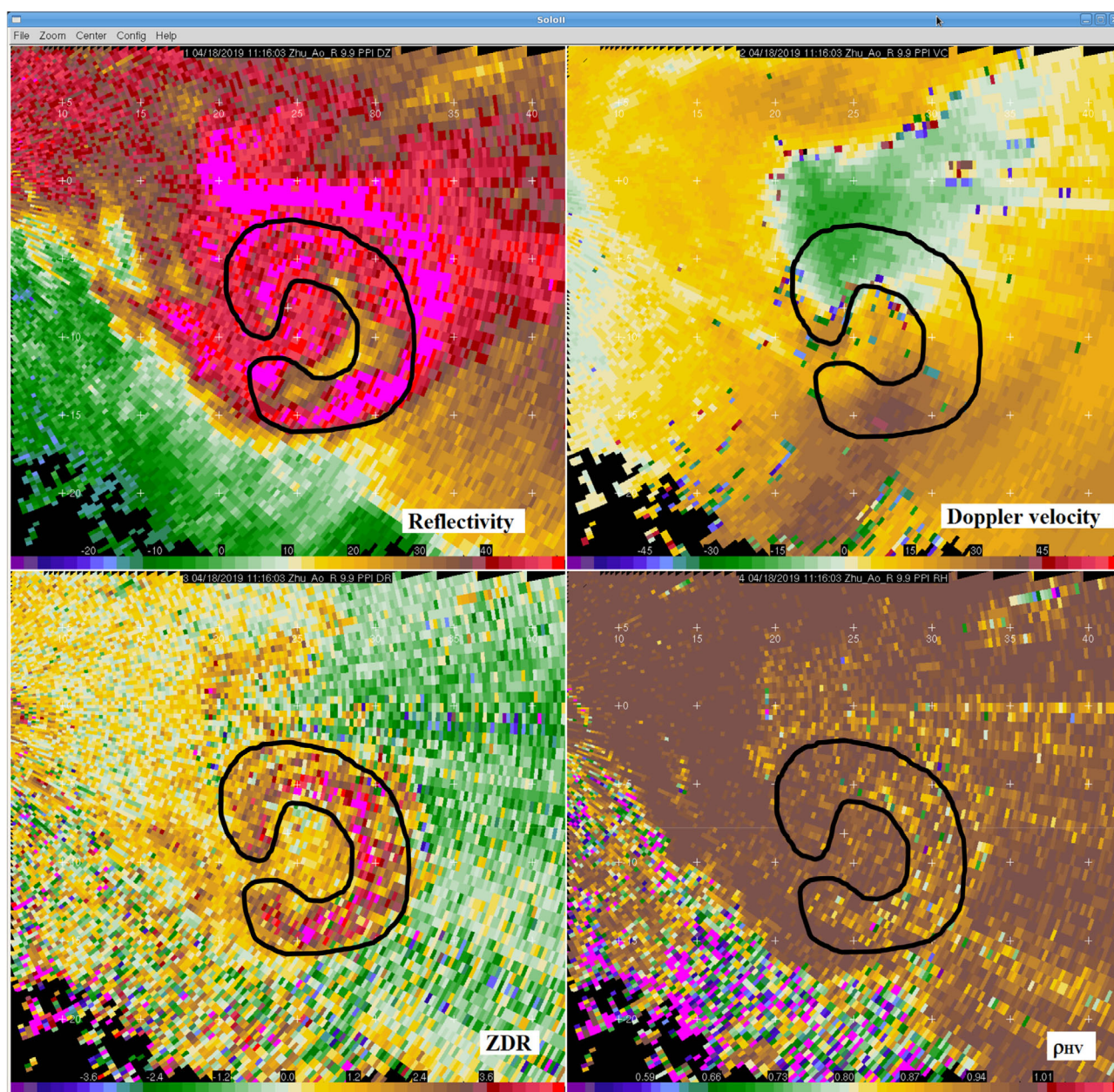


FIGURE 10 Ring-like structures in  $Z_{DR}$ ,  $\rho_{HV}$  aloft at 4.4 km above radar level. The area of high  $Z_{DR}$  is bounded by the black line



aloft can indicate the location of the updraft. This storm has pronounced  $Z_{DR}$  and slight  $\rho_{HV}$  rings aloft, as shown in Figure 10. These rings were apparent generally above a height of 4 km for the duration of the data.

### 5.3 | Reduction of $\rho_{HV}$ values within tornadoes lofting debris

Due to the lofting of debris, which tumbles and/or has varied orientation, there can be low  $\rho_{HV}$  associated with tornadoes. However, tornadoes/waterspouts occurring over water may not be associated with substantially reduced

$\rho_{HV}$  since they loft water drops, not debris (Kosiba et al., 2012). No such depression is clearly seen in the present case although at times there may be some weak depression, more likely associated with strong inflow and turbulence within the hook, visible in Figure 11.

## 6 | NUMERICAL WEATHER PREDICTION MODEL SIMULATION

This section describes the simulation results for this case using a 2-km resolution, near real-time configuration of the Weather Research and Forecast (WRF) model

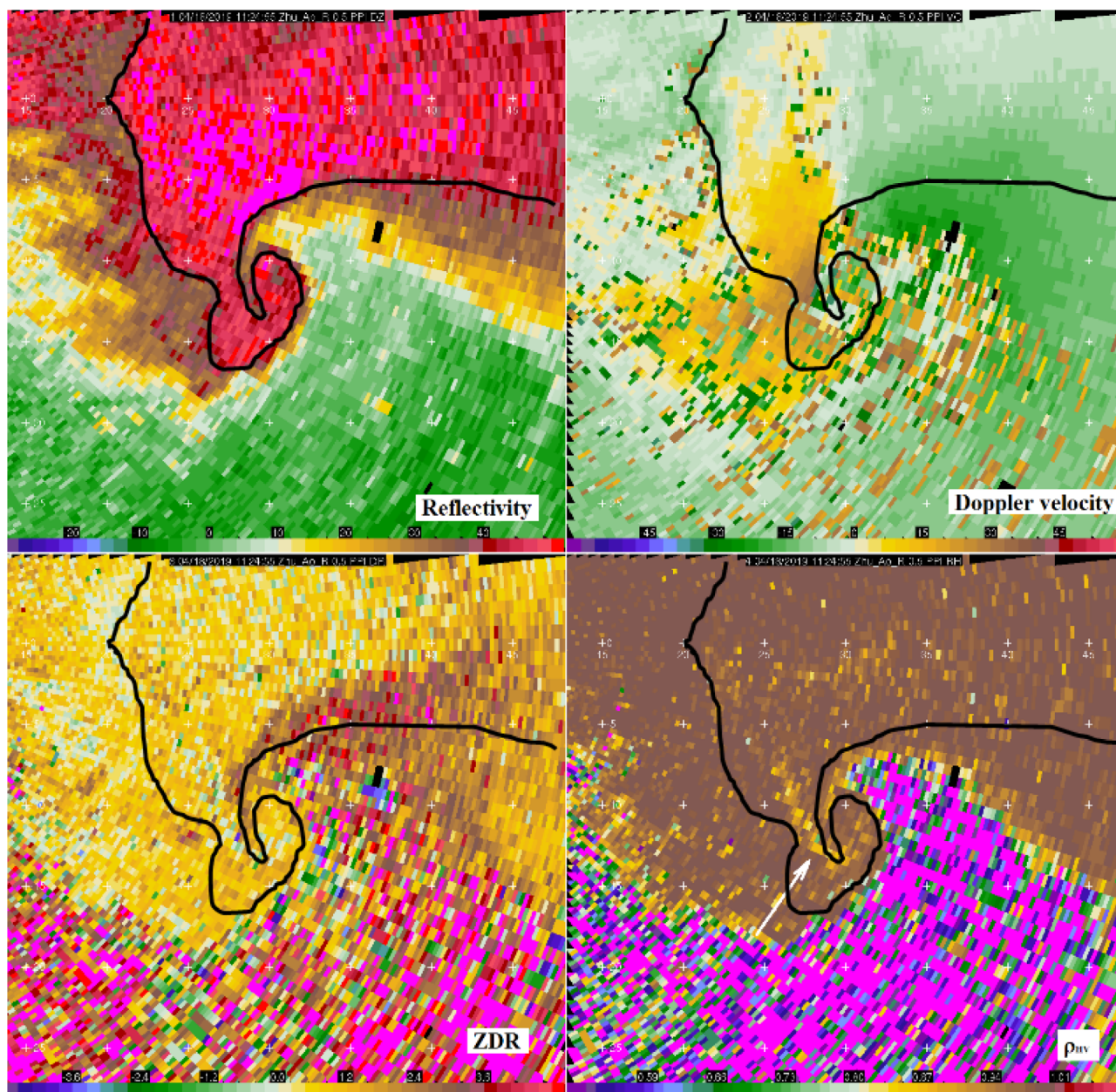
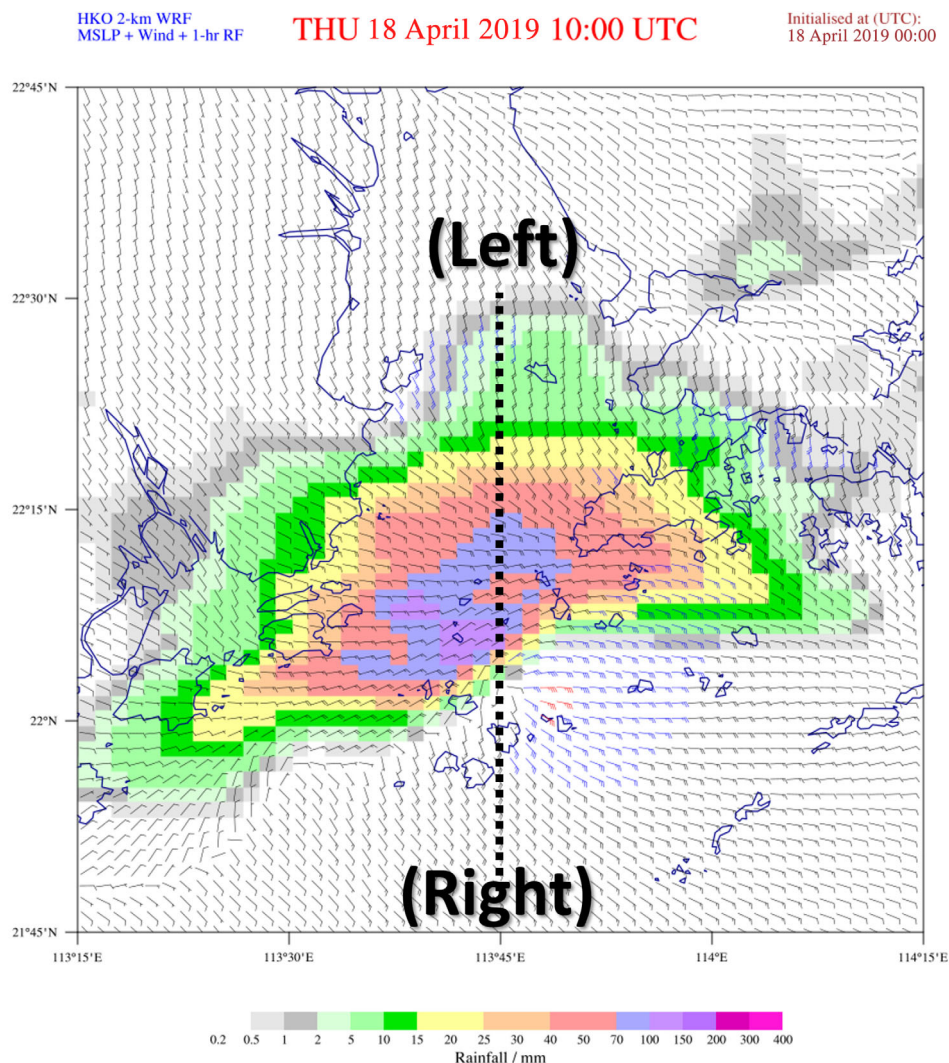


FIGURE 11 As in Figure 10, showing lower values of  $\rho_{HV}$  in the reflectivity hook, indicated by arrow. The highest reflectivity region of the hook and storm core is outlined in black

**FIGURE 12** Forecast 1-h rainfall and surface wind distribution around the Pearl River Estuary by the 2-km WRF model run. The model is initialized at 00 UTC on the day of the event. This is the 10-h forecast valid at 10 UTC. Wind barbs are coloured by wind strength (refer to the main text for description). The left and right refers to the left-hand side and right-hand side of the vertical cross section in Figure 13



(Skamarock & Klemp, 2007). Here the model domain comprises  $901 \times 901$  horizontal grid points, which are centred on Hong Kong and cover the region (14–30°N, 105–122°E). Vertically there are 42 levels, with at least 10 layers within the lowest 1 km and with the model top specified at 50 hPa at the time of initialization. Adaptive time stepping is used during integration, with the limiting Courant number set to 1.0 to ensure numerical stability. Typically an integration time step between 10 and 20 s is attainable, but during certain periods of active convection or high boundary layer, wind speeds decrease to around 6–8 s. Key model configurations include the WRF double-moment 6-class microphysics scheme (Lim & Hong, 2010), YSU planetary boundary layer scheme (Shin et al., 2013), Noah land surface model (Niu et al., 2011) and RRTMG schemes for long- and short-wave radiation (Iacono et al., 2008). Given the relatively fine horizontal grid-spacing, cumulus parameterization scheme is not used.

Previous studies in the same region have demonstrated the technical possibility of predicting the

convective storm cell or mesoscale/microscale rotation associated with an observed tornado or waterspout with a lead time of up to a couple hours (Chan et al., 2021; Hon et al., 2019, 2021). In these cases, the model employed was a 200-m resolution WRF configuration (Chan & Hon, 2016; Hon, 2020), which, while being able to reproduce many observed fine-scale airflow features, had a relatively small forecast domain ( $581 \times 581$  horizontal grid points covering an area of about  $112 \times 112 \text{ km}^2$  around Hong Kong) and short forecast range (up to 6–9 h). In the present study, the 2-km WRF configuration is used to examine the possibility of providing longer lead times.

The initial time is chosen at 00 UTC of the same day (i.e. 10–12 h before the event). To emulate real-time settings of an operational model run, the latest available ECMWF run (i.e. 12 UTC from the day before) is used to provide boundary and first guess initial conditions. Data assimilation is based on the 3-D variational scheme of WRF (WRFDA) and utilizes all conventional surface and upper-air observations within the forecast domain, as



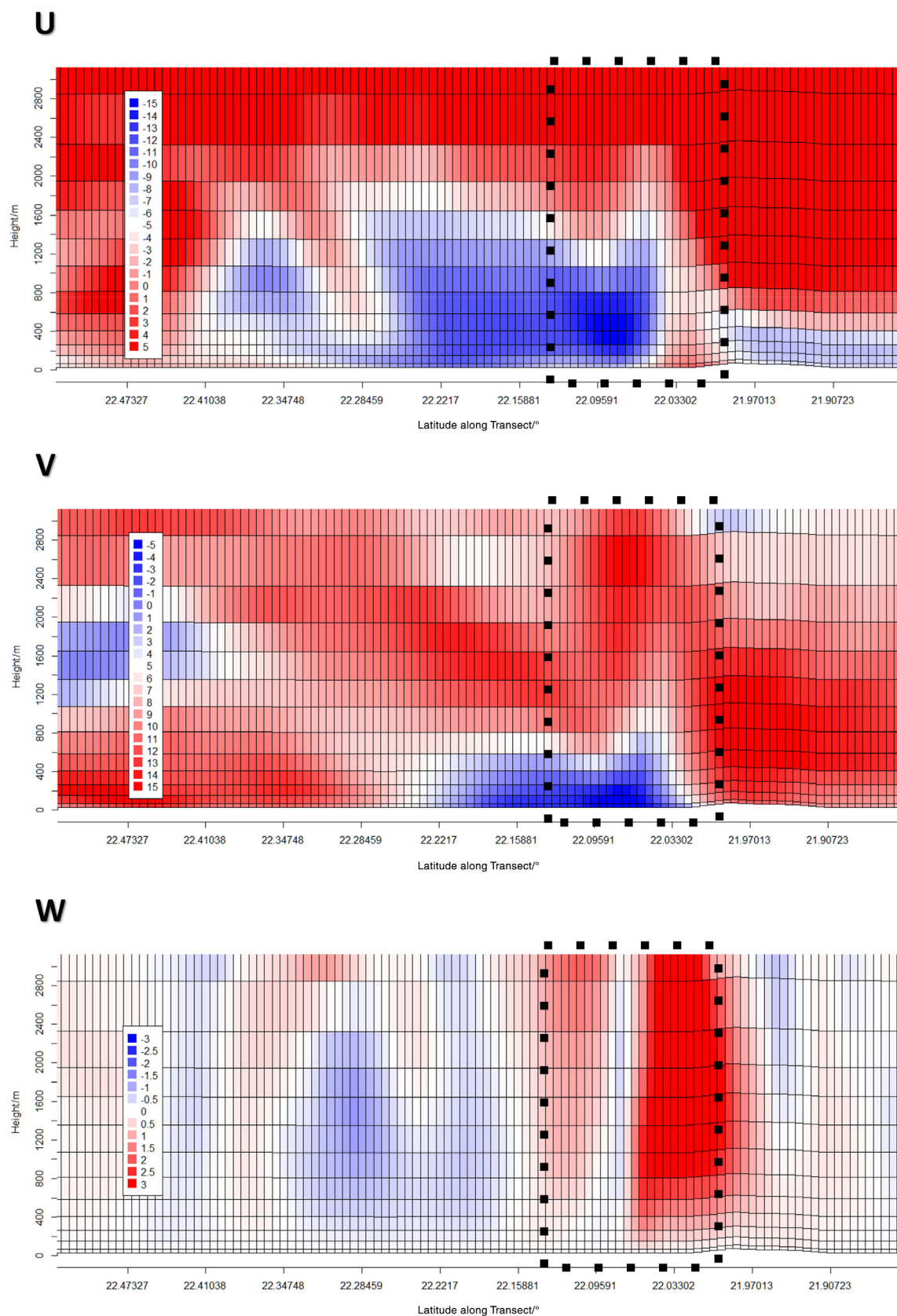


**FIGURE 13** Vertical cross sections taken along the thick dotted line in Figure 12. The same model run from the 2-km weather research and forecast as in Figure 12 is used. The four panels are respectively the horizontal wind components  $u$ ,  $v$ , vertical wind component  $w$  and simulated radar reflectivity. Position of the simulated features corresponding to a possible tornado supercell is highlighted

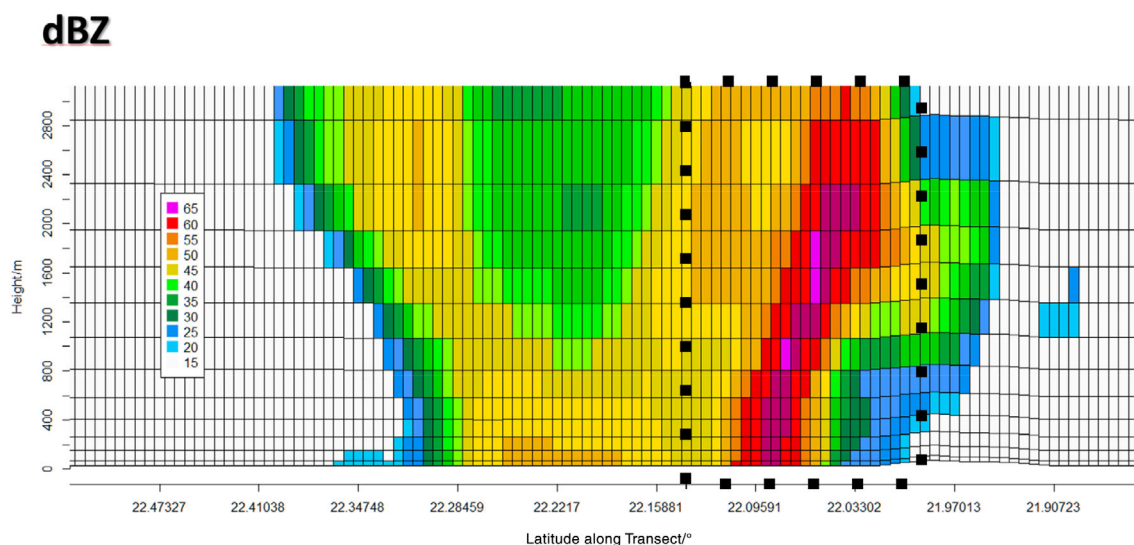


FIGURE 13 (Continued)

well as the dense surface observation network over inland Guangdong area operated by Guangdong Meteorological Service. While the assimilation of radar data through advanced ensemble-based methods have been shown to provide short-term forecast benefits in the region (Chiu & Hon, 2018; Hon & Kong, 2019), for the present case, the long forecast lead time required and the lack of radar echoes within observation range at the model initial time both do not favour the use of radar observations, which could be the subject of future studies.

Figure 12 shows the 10-h forecast from the 2-km WRF model run, valid at 10 UTC of the day of the event. The forecast chart shows the surface wind and 1-h rainfall distribution around the Pearl River Estuary region, with Hong Kong in the eastern half of the map display. An area of intense convective rainfall is predicted to the southwest of Hong Kong, with many model grid points giving 1-h rainfall over 50 mm (red pixels) and even 70 mm (purple pixels). The location, shape and size of the intense rainfall area appear to be generally consistent with the observed radar echoes. Examining the surface wind field, cyclonic flow can be seen at the south-eastern flank of the rain area, which also shows signs of an 'inflow notch' typical of supercell thunderstorms. The wind barbs highlighted in blue represent 10-m wind speeds between 11.4 and 17.5 m/s (force 6–7). There are also a few wind barbs highlighted in red, which represent 10-m wind speeds between 17.5 and 24.5 m/s (force 8–9). While the maximum of these is still considerably lower than the observed maximum gust at HMZ of 44.2 m/s, the model can still be said to provide indication of elevated surface wind strength associated with (and ahead of) the thunderstorm cluster.

To inspect the vertical structure of the simulated supercell, vertical cross sections are made along the dotted line in Figure 12. These are displayed in Figure 13. The four panels are, respectively, the horizontal wind components  $u$ ,  $v$ , vertical wind component  $w$  and simulated radar reflectivity. From the reflectivity cross section, an intense region of echoes exceeding 60 dBZ (purple or magenta pixels) can be seen near the leading edge of the storm cell. It is tilted forward along the direction of movement of the storm cell, and extends up to an altitude of about 2.5 km with an overhanging feature. Collocated with the dBZ column, features of rotation can be seen from the cross sections of  $u$  and  $v$ . In these two panels, an asymmetric colour scale has been used to remove the visual impact of the background airflow components. Here, a dipole pattern (changing from red to blue through white) can be observed to extend downwards from a height of about 2 km for  $u$ , and 1.5 km for  $v$ , to the surface at about the same location of the simulated overhanging echoes. These horizontal flow features also coincide with a strong updraft column (red pixels) in the cross section of  $w$ , which extends from the surface up to about 3 km in height. To the north (i.e. left) of this updraft column, there is also a narrow downdraft column (blue pixels) sandwiched by red updraft pixels on either side. It appears that, in the present case, the 2-km WRF model run is able to produce the salient features of the supercell thunderstorm with a lead time of 10–12 h.

## 7 | CONCLUSIONS

A supercell tornado/waterspout over south China coastal waters was documented for the first time. It occurred on

the evening of 18 April 2019 about 60 km south-southwest of Hong Kong. From a nearby surface weather station, the winds gusted to hurricane force for a few seconds when affected by this tornado/waterspout. Gusts of this strength had never been observed before in the region in association with thunderstorms.

The tornado/waterspout was well documented by the observations by the Zhu Ao radar. The DV was analysed using the GVBTD method and the vertical profile of the wind could have significant contributions to wind engineering applications in southern China. Dual-polarization observations of the waterspout/tornado have also been analysed and compared with similar supercell tornadoes observed in other parts of the world. Many features in common were observed. Such documentation would be unique for supercells over south China coastal waters.

Predictability of the supercell was analysed using the WRF model. The WRF model with sufficiently high spatial resolution was able to simulate the occurrence of the supercell. The results could be useful for earlier alerting of the vessels operating in the south China coastal waters.

More cases of supercell-associated waterspouts/tornadoes should be monitored in southern China and the adjacent waters and their properties documented in future studies.

## AUTHOR CONTRIBUTIONS

**P. W. Chan:** Conceptualization (equal); formal analysis (equal); investigation (equal); writing – original draft (equal); writing – review and editing (equal). **K. K. Hon:** Data curation (equal); formal analysis (equal); software (equal); writing – original draft (equal); writing – review and editing (equal). **Q. S. Li:** Conceptualization (equal); project administration (equal); supervision (equal). **J. Wurman:** Formal analysis (equal); investigation (equal); methodology (equal); software (equal). **P. Robinson:** Formal analysis (equal); investigation (equal); methodology (equal). **K. Kosiba:** Investigation (equal); methodology (equal); software (equal); visualization (equal).

## ORCID

P. W. Chan  <https://orcid.org/0000-0003-2289-0609>

K. K. Hon  <https://orcid.org/0000-0002-4842-0843>

## REFERENCES

- Chan, P.W. & Hon, K.K. (2016) Performance of super high resolution numerical weather prediction model in forecasting terrain-disrupted airflow at the Hong Kong international airport: case studies. *Meteorological Applications*, 23, 101–114. <https://doi.org/10.1002/met.1534>
- Chan, P.W., Hon, K.K., Robinson, P., Kosiba, K., Wurman, J. & Li, Q.S. (2021) Analysis and numerical simulation of a waterspout at the Hong Kong International Airport. *Meteorologische Zeitschrift*, 30, 333–348.
- Chen, J., Cai, X., Wang, H., Kang, L., Hongshen Zhang, Y., Song, H.Z. et al. (2017) Tornado climatology of China. *International Journal of Climatology*, 38, 2478–2489.
- Chiu, Y. Y. & Hon, K. K. (2018) First studies on mesoscale ensemble data assimilation over the South China coastal areas. *The 32nd Guangdong-Hong Kong-Macau Meteorological Technical Seminar, 8–10 January 2018, Macau*. <https://www.hko.gov.hk/en/publica/reprint/files/r1343.pdf> (Chinese only with English abstract).
- Crowe, C.C., Petersen, W.A., Carey, L.D. & Cecil, D.J. (2010) A dual-polarization investigation of tornado-warned cells associated with hurricane Rita (2005). *Electronic Journal of Operational Meteorology*, 11(4).
- Dawson, D.T., II, Mansell, E.R. & Kumjian, M.R. (2015) Does wind shear cause hydrometeor size sorting? *Journal of the Atmospheric Sciences*, 72(1), 340–348.
- Hon, K.K. (2020) Predicting low-level windshear using 200-m resolution NWP at the Hong Kong international airport. *Journal of Applied Meteorology and Climatology*, 59, 193–206. <https://doi.org/10.1175/JAMC-D-19-0186.1>
- Hon, K.K. & Kong, W., 2019: Convective-scale Cycling Ensemble Data Assimilation using Rapid Scan Observations from the Tai Mo Shan Weather Radar. *The 33rd Guangdong-Hong Kong-Macau Meteorological Technical Seminar, 6–8 March 2019, Hong Kong*. <https://www.hko.gov.hk/en/publica/reprint/files/r1357.pdf> (Chinese only with English abstract).
- Hon, K.K., Tse, S.M., Chan, P.W. & Li, Q.S. (2019) Observation and real-time simulation of a tornado event in Hong Kong on 29 August 2018. *Advances in Meteorology*, 2019, 8571430, 13 pages. <https://doi.org/10.1155/2019/8571430>
- Hon, K.K., Tse, S.M., Chan, P.W. & Li, Q.S. (2021) Observation and numerical simulation of a weak waterspout at Hong Kong international airport. *Meteorological Applications*, 28, e1975. <https://doi.org/10.1002/met.1975>
- Iacono, M.J., Delamere, J.S., Mlawer, E.J., Shephard, M.W., Clough, S.A. & Collins, W.D. (2008) Radiative forcing by long-lived greenhouse gases: calculations with the AER radiative transfer models. *Journal of Geophysical Research*, 113, D13103.
- Kosiba, K.A., Wurman, J., Robinson, P., Schwarz, C., Burgess, D. W., Mansell, E.R. et al. (2012) Mobile radar observations and damage assessment of the 24 May 2011, Canton Lake, OK tornado. *AMS 26th conference on severe local storms, Nashville, TN*.
- Kumjian, M.R. & Ryzhkov, A.V. (2008) Polarimetric signatures in supercell thunderstorms. *Journal of Applied Meteorology and Climatology*, 47(7), 1940–1961.
- Kumjian, M.R. & Ryzhkov, A.V. (2012) The impact of size sorting on the Polarimetric radar variables. *Journal of the Atmospheric Sciences*, 69(6), 2042–2060.
- Lam, H.Y., Lee, S.M. & Hon, K.K. (2018). Latest Development of the Guangdong-Hong Kong-Macau Lightning Location Network and Data Analysis Related to Super Typhoon Hato. *The 32nd Guangdong-Hong Kong-Macau Meteorological Technical Seminar, 8–10 January 2018, Macau*. <https://www.hko.gov.hk/en/publica/reprint/files/r1337.pdf> (Chinese only with English abstract).



- Lee, W.C., Jou, B., Chang, P. & Deng, S. (1999) Tropical cyclone kinematic structure retrieved from single-Doppler radar observations. Part I: interpretation of Doppler velocity patterns and the GBVTD technique. *Monthly Weather Review*, 127, 2419–2439.
- Lim, K.-S.S. & Hong, S.-Y. (2010) Development of an effective double-moment cloud microphysics scheme with prognostic cloud condensation nuclei (CCN) for weather and climate models. *Monthly Weather Review*, 138, 1587–1612.
- Loeffler, S.D. & Kumjian, M.R. (2018) Quantifying the separation of enhanced ZDR and KDP regions in nonsupercell tornadic storms. *Weather and Forecasting*, 33(5), 1143–1157.
- Martinaitis, S.M. (2017) Radar observations of tornado-warned convection associated with tropical cyclones over Florida. *Weather and Forecasting*, 32(1), 165–186.
- Niu, G.Y., Yang, Z.-L., Mitchell, K.E., Chen, F., Ek, M.B., Barlage, M. et al. (2011) The community Noah land surface model with multiparameterization options (Noah-MP): 1. Model description and evaluation with local-scale measurements. *Journal of Geophysical Research*, 116, D12109.
- Shin, H.H., Hong, S., Noh, Y. & Dudhia, J. (2013) Derivation of turbulent kinetic energy from a first-order nonlocal planetary boundary layer parameterization. *Journal of the Atmospheric Sciences*, 70(2013), 1795–1805. <https://doi.org/10.1175/JAS-D-12-0150.1>
- Skamarock, W.C. & Klemp, J.B. (2007) A time-split nonhydrostatic atmospheric model for weather research and forecasting applications. *Journal of Computational Physics*, 227(2008), 3465–3485.

**How to cite this article:** Chan, P. W., Hon, K. K., Robinson, P., Kosiba, K., Wurman, J., & Li, Q. S. (2022). Analysis and numerical simulation of a supercell tornado at the Hong Kong adjacent waters. *Meteorological Applications*, 29(2), e2056. <https://doi.org/10.1002/met.2056>